JOURNAL OF THERMOPHYSICS AND HEAT TRANSFER
Vol. 8, No. 3, July–Sept. 1994

Measurements of Ultraviolet Radiation from a 5-km/s Bow Shock

Peter W. Erdman* and Edward C. Zipf†
University of Pittsburgh, Pittsburgh, Pennsylvania 15260
Patrick Espy‡ and L. Carl Howlett§
Utah State University, Logan, Utah 84322
Deborah A. Levin¶
Institute for Defense Analyses, Alexandria, Virginia 22311
and
Robert J. Collins** and Graham V. Candler††
University of Minnesota, Minneapolis, Minnesota 55455

Ultraviolet emission from a 5.1-km/s re-entry bow shock was measured in a sounding rocket experiment launched from the Barking Sands Research Range (Kauai, Hawaii) in February 1991 at 14:30 GMT. Optical data were obtained on the downleg portion of the flight as the payload descended from 115 to 62 km in a very shallow trajectory at a nearly constant speed. The intensity of the ultraviolet spectrum (λ200–400 nm), and the vacuum ultraviolet resonance radiation emitted by atomic oxygen and hydrogen at λ130.4 nm and λ121.5 nm, respectively, were measured. Data from optical instruments in the 200–400-nm spectral region is presented here. Langmuir probe measurements provided data on the total plasma density and electron temperature in the boundary layer over a limited altitude range.

Introduction

THE uv diagnostics experiment (UVDE) was developed to validate aerodynamic and radiative transfer models applicable to re-entry conditions, and to measure the intensity and spectral distribution of the ultraviolet radiation emitted by the Antares II and Star 27 engine plumes. This flight was the second in a series of bow shock experiments.[1,2] Previous papers[3,4] have described the payload instrumentation, data, and modeling for the engine plume measurements obtained during this second flight. This article will describe the re-entry bow shock data obtained, with a brief description of the instrumentation. A companion set of articles[5,6] discuss the flow and radiation analyses for the re-entry data presented here.

The UVDE payload was divided into forward and aft instrumentation sections which observed the re-entry bow shock and motor plumes, respectively. A similar scanning uv spectrometer and multiple filtered photometers were contained in each section.

The geometry of the flight was optimized to give the maximum data acquisition time for the bow shock measurements by re-entering at a very shallow angle. This was accomplished by having the first-stage Castor I booster lift the payload to an altitude of approximately 120 km. An attitude control system was then used to pitch the payload down a few degrees from the horizontal during the Antares II second-stage and Star 27 third-stage engine burns. These upper stage burns accelerated the payload to the re-entry velocity of 5.1 km/s, nearly tangential to the atmosphere at the 100-km point. The vertical component of the speed was approximately 0.8 km/s, so that a significant increase in the data acquisition time was achieved relative to a simple ballistic trajectory. The rocket trajectory during the re-entry time portion of flight is shown in Fig. 1.

The first significant bow shock emission observed was in the OH(A → X) bands at approximately an altitude of 110 km and a speed of about 4 km/s while the payload was still accelerating during the Star 27 burn. Data collection continued until approximately 62 km when the payload was destroyed by structural failures due to re-entry heating. The aluminum dome and aluminum honeycomb skin were designed for maximum weight reduction to achieve the highest re-entry speed possible.

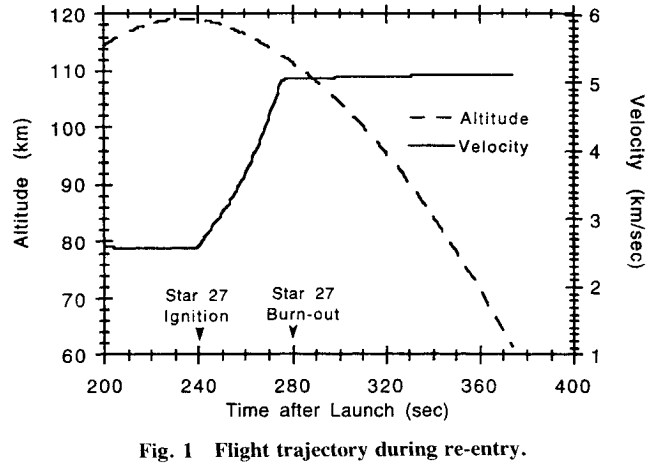

Fig. 1 Flight trajectory during re-entry.

Presented as Paper 92-2870 at the AIAA 27th Thermophysics Conference, Nashville, TN, July 6–8, 1992; received June 16, 1993; revision received Oct. 5, 1993; accepted for publication Oct. 6, 1993.

*Research Associate Professor, Department of Physics and Astronomy. Member AIAA.
†Professor, Department of Physics and Astronomy. Member AIAA.
‡Research Associate Professor, Department of Physics.
§Technical Program Manager, Center for Space Engineering. Member AIAA.
¶Research Staff Member, Science and Technology Division. Member AIAA.
**Professor, Department of Electrical Engineering.
††Assistant Professor, Department of Mechanical and Aerospace Engineering. Member AIAA.

Payload Instrument Description

The bow shock instrumentation on the payload consisted of the following forward viewing selection of instruments: a rapid scan spectrometer, eight quartz fiber optic photometers, an electron density microprobe, and two VUV photometers. Numerous temperature monitors provided support information about the total heat loading on the dome covering these instruments. Figure 2 shows the arrangement of the instrumentation in the payload and the location of the viewing windows. The spectrometer and photometers were designed to provide both overlapping and complementary data in order to maximize the data set acquired, provide redundancy in case of a failure, and as a consistency check on the final data.

The rapid scanning spectrometers covered the λ190–400-nm wavelength range in a 1.0-s scan. These instruments were a modified Fastie-Ebert design of 150-mm focal length, with a 10-deg (total angle) field of view (FOV) centered on the vehicle centerline for the forward-viewing instrument. This spectrometer was used to measure the bow shock ultraviolet radiance near the stagnation point—primarily from the nitric oxide gamma band system, but also from the OH(A-X) bands. Further spectrometer instrument specifications are given in Refs. 1 and 3. The accuracy of the spectrometer absolute radiance measurements is generally within $\pm 20\%$.

A modest scan speed of 1 s/scan gave better than 1 km of altitude resolution at the planned shallow re-entry. Model predictions indicated that the signal levels on re-entry would cover a wide dynamic range, hence, good altitude resolution and total instrumental dynamic range were very important for a successful measurement. Due to the difficulty in predicting both the radiance levels and the vehicle performance for this flight, no detector gain changes were programmed—unlike the first bow shock experiment where this technique was used to increase the dynamic range by several more orders of magnitude.

The filtered photometers were located on inner decks in the payload and were coupled to the forward windows with quartz fiber optics. The photocathodes were selected according to the spectral feature of interest. Like the spectrometer system, these individual detectors also had both an analog electrometer channel and a digital pulse counting channel in order to increase the total dynamic range to approximately seven orders of magnitude. The variations in intensity with position from the stagnation point was also measured by separate photometers with viewing angles of 0, 30, and 50 deg from the vehicle centerline. The total angle of the entrance FOV of each photometer was ~25 deg. The emission feature identified with each photometer and the viewing angle of each instrument is given in Table 1. Additional photometer instrument specifications are given in Refs. 1 and 3. The absolute radiometric accuracy of the photometers is similar to that of the spectrometers.

The payload also included the atomic oxygen [OI λ130.4 nm] and hydrogen [HI λ121.5 nm] vacuum ultraviolet (VUV) sensors which were located on the dome ~40 deg from the vehicle's centerline. Significant fluxes were observed by these detectors during re-entry, indicating that large VUV fluxes reach the surface of the vehicle. The data and its interpretation requires analyses different than those used in the examination of the UV radiation, and are discussed elsewhere.[7]

A simple langmuir microprobe module was used to measure the electron density and temperature in the bow shock during re-entry. The guarded probe wire was 5-mm long and 0.5 mm in diameter, located on the dome at ~45 deg from the vehicle's centerline. The probe's potential was varied linearly in time by a symmetrical voltage sweep with a 0.2-s period, scanning from -1 to $+4$ V with respect to the guard electrode. A differential electrometer amplifier measured the probe current, which was then digitized by a fast 16-bit A/D converter, yielding individual current and probe potential measurements with 100-μs resolution. The electron temperature was deduced from the variation of the probe current during the retarding potential portion of the sweep, while the electron and positive ion densities could be independently measured from the electron and ion saturation currents. These data will provide useful comparison with the theoretically calculated values of these parameters.

Absolute calibrations for both the spectrometer and the photometers were performed with a deuterium lamp. Cross calibrations were also performed in the field under identical conditions to minimize the systematic errors. Separate transmission calibrations of the quartz viewing windows in the dome were performed on the actual flight windows, and finally an end-to-end calibration was performed with the uv instruments installed in the payload and using the telemetered data. All of these calibration efforts were intercompared to check for any inconsistencies which might reveal potential errors.

Table 1 Photometer characteristics

Spectral features	$\lambda_c \pm \Delta\lambda$[a]	Forward viewing angle[b]	Azimuth angle
NO	215 ± 3	0	0
NO	230 ± 25.5	0	0
NO	230 ± 25.5	30	285
NO	230 ± 25.5	50	285
N_2^+	391 ± 1.25	0	0
OH	310 ± 4	0	0
OH	310 ± 4	30	105
OH	310 ± 4	50	105

[a]Center wavelength and filter bandwidth at half-power transmission in nm.
[b]Angles given in degrees. The forward viewing angle is the same as the dome angle.

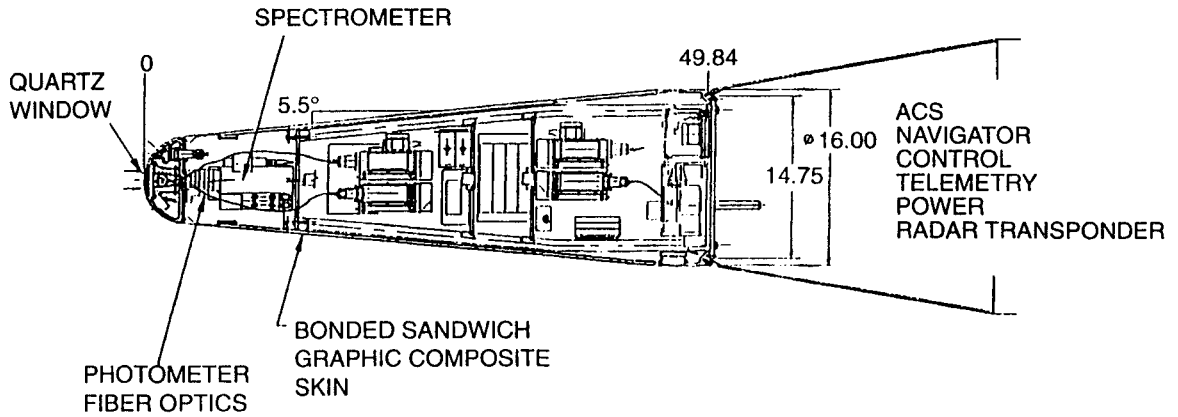

Fig. 2 Simplified schematic diagram showing the location of the optical instrumentation and microprobe on the UVDE payload.

No vacuum system was employed, therefore, the spectrometer data acquired below λ200 nm will not be presented here due to absorption uncertainties. Spectral line sources were used to properly locate the spectrometer wavelength scan and establish the wavelength interval. The VUV gas diodes were compared against a National Bureau of Standards-calibrated VUV diode to yield an absolute calibration for the oxygen λ130.4-nm and hydrogen λ121.5-nm measurements. The microprobe was calibrated in a laboratory plasma system where the electron density and temperature could be measured using other independent techniques, and cross compared with the microprobe.

The entire payload was hermetically sealed and remained pressurized during the flight. Before launch, the payload was vigorously purged and then positively pressurized with dry Argon. This gas then continued to flow out the small viewing ports used for the VUV measurements, thereby reducing the absorption of that radiation. Reference 7 discusses the adequacy of the purge technique employed.

Spectrometer Data

All the payload instrumentation and supporting diagnostics performed nominally throughout the flight. The selected instrument sensitivities proved to be nearly optimal for acquiring data over the altitude regime of interest. The observed radiation increased rapidly as the payload descended, although the velocity increased only slightly (0.1 km/s). Figures 3 and 4 show the uv spectra obtained from the forward-viewing spectrometer. The single-scan data in Fig. 3 shows the uv bow shock spectrum at altitudes of 89.7, 87.5, 85.1, 79.0, and 76.4 km during re-entry. This spectrum is dominated by NO(A-X) gamma band emission. Figure 4 is the sum of five scans at an average altitude of 100 km, and in contrast to Fig. 3, shows the OH(A-X) bands (primarily 1,0 and 0,0), with little or no NO gamma band emission. Saturation begins to affect portions of the spectrometer data at altitudes below ~75 km, although data collection continued until payload destruction near 60 km.

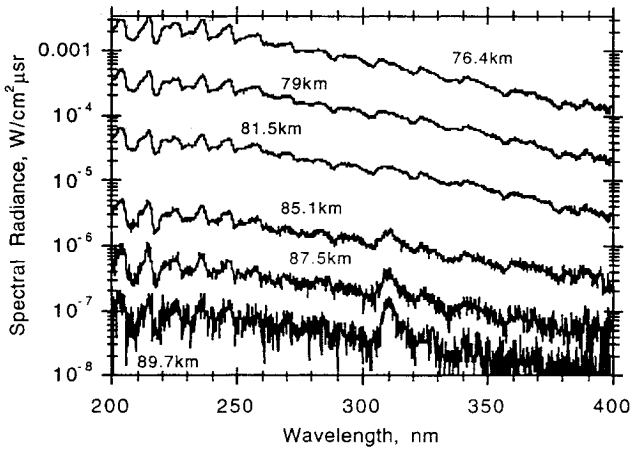

Fig. 3 Spectral scans of the ultraviolet bow shock radiation taken during re-entry.

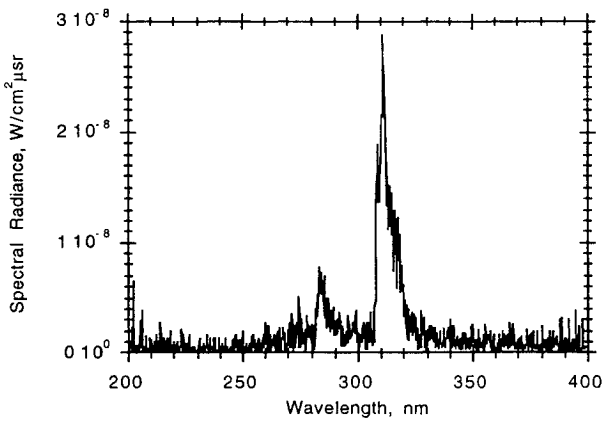

Fig. 4 Ultraviolet spectrum of the re-entry bow shock at an average altitude of 100 km.

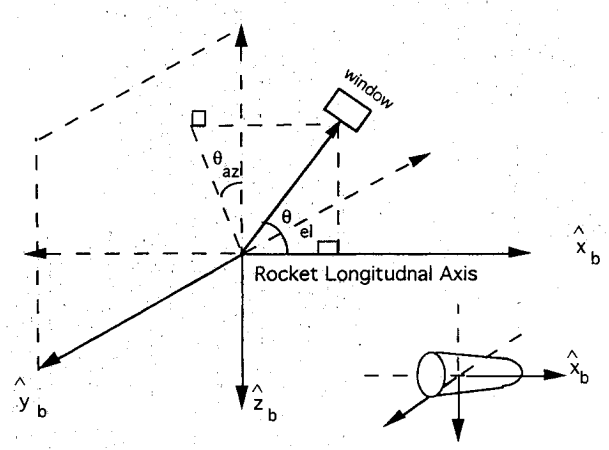

Fig. 5 Onboard instruments defined in the rocket body frame coordinate system.

Photometer Data

Table 1 gives the respective spectral features, center wavelength, full width at half maximum of the photometer passband, and the viewing angles. Good data were obtained, although work was required to remove the effects of spin modulation. That analysis and data are described here.

Complete stage separation was achieved after the second-stage burnout; however, the spent second stage caught up with, and bumped the third stage. Although the payload was spin stabilized, this interaction introduced an unbalanced force which caused the payload to precess as the rocket entered the sensible atmosphere.

The effect of the rocket precession on the radiances obtained from bow shock 2 is noticeable in the photometer data, particularly for the off-axis instruments. This body motion needs to be accounted for so that quantitative comparisons can be made with flow and radiance models. In addition to the standard information, such as speed and altitude, data users also need to know the angle between a given sensor and the effective stagnation streamline γ as a function of time. Using the measured body frame velocity components[8] and the location of the onboard instruments in the body, reference frame γ can be found. Figure 5 shows the relationship between the dome θ_{el} and azimuth θ_{az} angles used in Table 1 and a spherical coordinate system centered at the nose radius. The body frame unit vectors, $\hat{x}_b$, $\hat{y}_b$, and $\hat{z}_b$, are related to θ_{el} and θ_{az} as

$$\begin{aligned} \hat{x}_b &= \cos\theta_{el} \\ \hat{y}_b &= \sin\theta_{el}\sin\theta_{az} \\ \hat{z}_b &= -\sin\theta_{el}\cos\theta_{az} \end{aligned} \tag{1}$$

Figure 6 shows the convention used to represent the body motion angles and velocity coordinates in the body reference frame.[8] The pitch α, yaw β, and total angle of attack α_{tot} angles are related to the velocity vector v_b in the body reference frame as

$$\begin{aligned} \alpha &= \tan^{-1}\left[\frac{-v_z^b}{\sqrt{(v_x^b)^2+(v_y^b)^2}}\right] \\ \beta &= \tan^{-1}\left(\frac{v_y^b}{v_x^b}\right) \\ \alpha_{tot} &= \tan^{-1}\left[\frac{\sqrt{(v_y^b)^2+(v_z^b)^2}}{v_x^b}\right] \end{aligned} \tag{2}$$

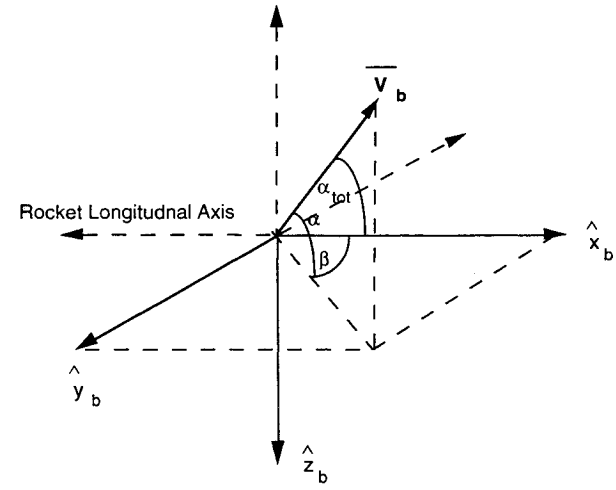

Fig. 6 Velocity and angle-of-attack definitions in body frame coordinate system.

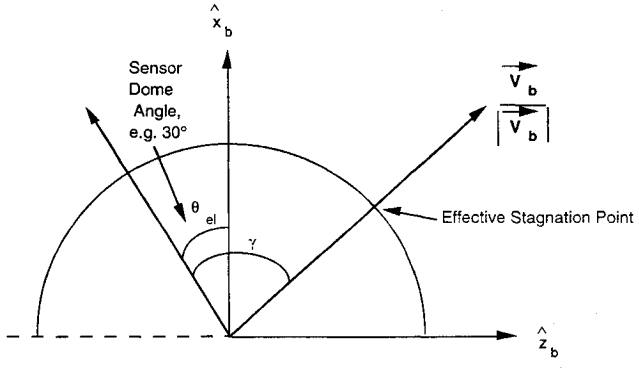

Fig. 7 Onboard instruments and directional wind vector defined in body frame coordinate system.

The unit vector of the relative wind is given as

$$\frac{\boldsymbol{v}_b}{|\boldsymbol{v}_b|} = \begin{bmatrix} \cos\alpha\cos\beta \\ \cos\alpha\sin\beta \\ -\sin\alpha \end{bmatrix} \tag{3}$$

Figure 7 shows the rocket geometry with the unit relative wind vector as measured in the body reference frame [Eq. (3)] and the angle between the instrument and the longitudinal axis of the rocket θ_{el}. If the velocity vector were aligned with the rocket longitudinal axis $\hat{x}_b$, then the angle between the stagnation streamline and θ_{el} would be the "forward viewing" or the dome angle as given in Table 1. For the flight data, this is not the case, and the direction of the wind vector changes as a function of time as shown in Fig. 7. To compare measured radiances levels with calculations, the angle between the effective stagnation point and the instrument γ can be computed as

$$\cos\gamma = \frac{\boldsymbol{v}_b}{|\boldsymbol{v}_b|} \cdot (\hat{x}_b, \hat{y}_b, \hat{z}_b) \tag{4}$$

The time dependence of γ should correlate with radiance time variation.

Figure 8 shows a comparison of the radiances obtained from the narrow band NO with that of the OH forward-viewing photometer. The altitude dependence of the NO to OH ratio observed is similar to that seen in the spectral scans of Fig. 3. The OH production rate is favored at lower densities relative to that of NO. This is also consistent with what was observed in the first bow shock flight experiment.[1,2]

Of the photometers listed in Table 1, the data from the NO photometers centered at 230 nm was the primary data set of

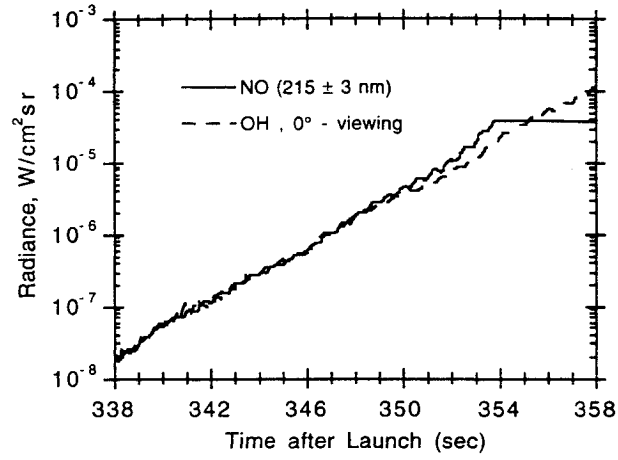

Fig. 8 Comparison of radiances from NO (215 ± 3 nm) with OH (310 ± 4 nm) forward-viewing photometers.

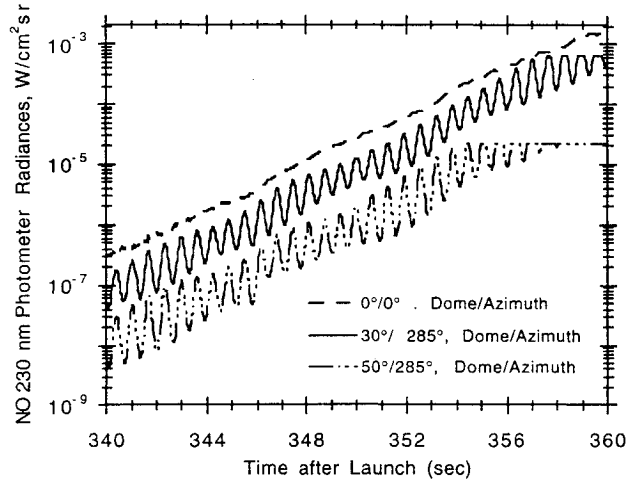

Fig. 9 Comparison of NO 0-, 30-, and 50-deg 230-nm photometer radiances as a function of time after launch during re-entry.

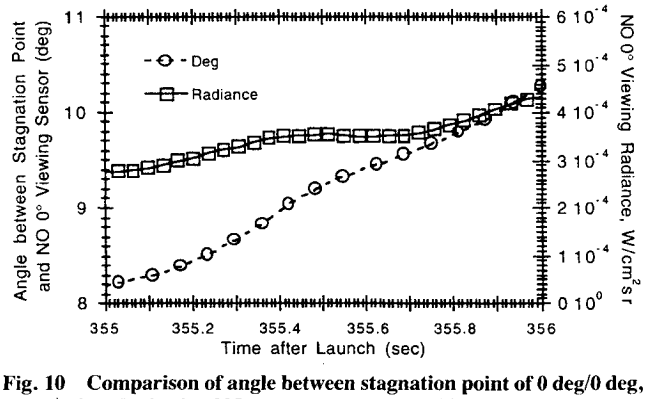

Fig. 10 Comparison of angle between stagnation point of 0 deg/0 deg, dome/azimuth viewing NO sensor centered at 230 nm and radiance as a function of time—late re-entry.

interest. That data will be analyzed and presented here; however, data from the other photometers may be obtained from the AEDC Plume Data Center, Arnold AFB, Tennessee. Figure 9 shows a comparison of the 0-, 30-, and 50-deg photometer radiances as a function of time after launch during re-entry. The spin modulation is seen to be worse for the off-axis photometers; and, is visible even in the 0-deg viewing instrument. The 30- and 50-deg photometers are seen to saturate at later times; although, some signal levels during saturated portions of the spin cycle can be estimated from information about the angular dependence of the signal. The saturation is due to higher signal levels obtained by viewing portions of the flow that are closer to the stagnation point

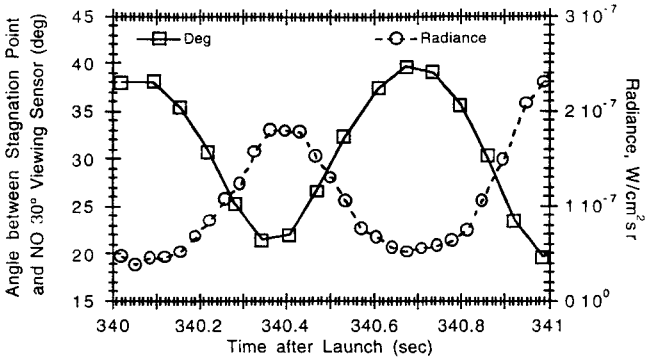

Fig. 11 Comparison of angle between stagnation point of 30 deg/285 deg, dome/azimuth viewing NO 230-nm sensor and radiance as a function of time—early re-entry.

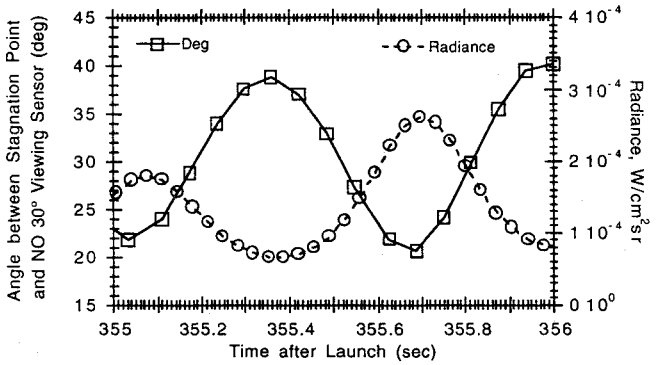

Fig. 12 Comparison of angle between stagnation point of 30 deg/285 deg, dome/azimuth viewing NO 230-nm sensor and radiance as a function of time—late re-entry.

than anticipated preflight. Figures 10–12 compare the time-dependent angle between the stagnation point and the sensor γ and the radiance data. Figure 10 shows that the so-designated 0-deg viewing instruments never looks at the stagnation point, but rather at an average value of 10 ± 2 deg. In the companion theory articles,[5,6] we compare this data with calculations that assume that the instrument was looking 0 deg from the rocket axis. Comparison of radiance calculations done at 0- and 10-deg off-axis showed only an average difference of 6% for altitudes between 55–88 km. Hence, the off-set of the "0-deg" photometer data does not affect the data interpretation. The modulation in signal and γ is slow and smooth, and the two are well-correlated. The photometer radiance only changes by ~1.6 over the spin period, which is on the order of a single spectrometer scan. The spectrometer is a wavelength scanning instrument; so that, the spin modulation cannot be as easily removed from that data. Hence, the minimal change in broadband radiance removes uncertainty about the effects of modulation in the interpretation of the spectral data. Figures 11 and 12 show enlargements of a single cycle at the beginning and end of the re-entry for the 30-deg viewing NO photometer. The radiance peaks at small γ (i.e., closer to the stagnation point) and is reduced at the largest values (i.e., towards the wake). Therefore, the time correlation appears to be good and provides detailed information on the angular radiance variation in the flow, as shown in Ref. 5.

Comparison of Spectrometer and Photometer Data

The self-consistency of data from the forward-viewing spectrometer and the 230-nm photometer was examined. Three sets of points in Fig. 13 represent the 230-nm photometer data and two types of derived spectroscopic measurements. Under the first flight conditions, the NO(0, 2) spectral peak at 215 nm showed the same altitude dependence as the 230-nm photometer data. Figure 13 shows that this trend also holds for

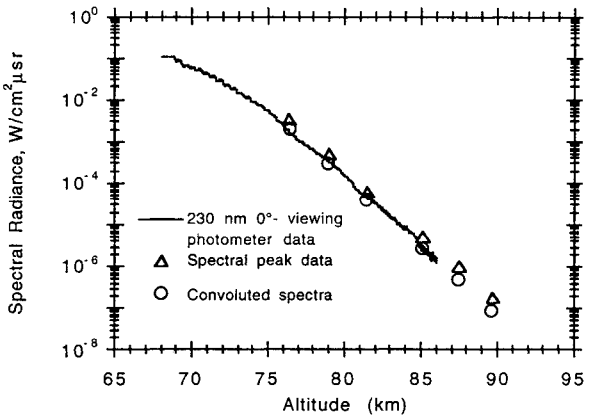

Fig. 13 Comparison of data from the forward-viewing spectrometer and the 230-nm photometer.

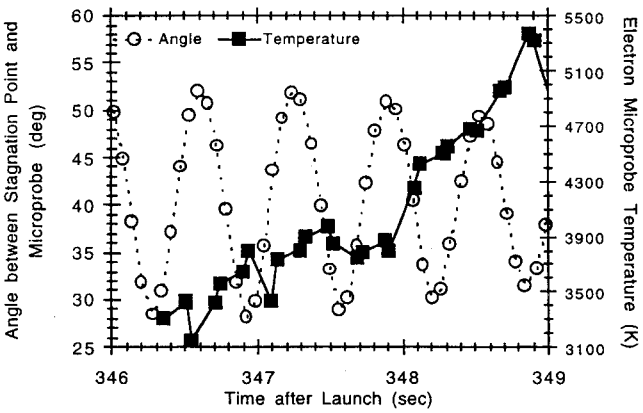

Fig. 14 Electron temperature obtained from the microprobe sensor and angle from the stagnation point (located at 40 deg/195 deg, dome/azimuth) as a function of time after launch.

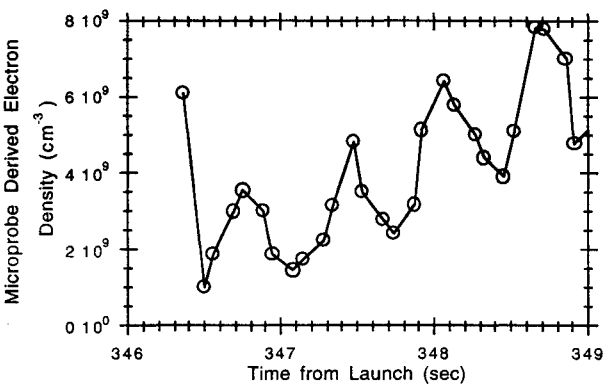

Fig. 15 Electron number density obtained from the microprobe sensor as a function of time after launch.

the second flight. In addition, spectra obtained at several altitudes were convolved with the photometer system response function. These results are designated as "convolved spectra" and show consistency with the other experimental results. Thus, within a factor of about 2, the spectrometer and photometer data sets are consistent. Differences in the viewing angle that were exacerbated by the rocket precession and spectrometer scan time of about 2 s can account for the small discrepancies observed.

Electron Microprobe Data

Figures 14 and 15 are the electron temperatures and densities measured by the microprobe between the altitudes of 81 and 79 km, near the altitudes where the spectra are shown in Fig. 3. The effects of spin modulation due to the vehicle's angle of attack are obvious in both the temperature and the

density. Due to the length of the probe measurement time it is probably not possible to remove the modulation in these data. At yet lower altitudes, the microprobe wire finally heats and becomes an electron emitter. Although the probe is still physically intact, this heating halts further useful data acquisition from this channel. The data between 81 and 79 km, however, provide a useful indication of the temperatures and densities of electrons in this weakly ionized flow.

Conclusions

The flight experiment obtained optical data from altitudes of 115 to 62 km for a constant rocket speed of 5.1 km/s. Spectrometer measurements from 200 to 400 nm of the shock-heated air in front of the vehicle indicated that the primary radiators were NO and OH. Photometer measurements were also obtained in the same spectral region. Although that data evidenced spin modulation effects, the radiance could be correlated with the instantaneous angle between the stagnation point and the sensor. Auxiliary data were obtained from an electron microprobe, VUV ionization chambers, and thermocouple measurements.

The data continue to provide an opportunity to test for the first time the computational fluid dynamics and radiation models that were originally developed for a higher-speed flight regime. References 5 and 6 discuss the challenge of predicting the NO radiance data that were shown in this article.

Acknowledgments

The UVDE was supported by the Innovative Science and Technology Office of the Ballistic Missile Defense Organization. The design, construction, and calibration of the payload instrumentation involved a collaborative effort among many institutions with Utah State University, Logan, Utah, serving as overall program manager for the instrument package. Utah State University also developed and fabricated the filtered photometers and the atomic oxygen [OI λ130.4 nm] and hydrogen [HI λ121.5 nm] VUV sensors. The University of Pittsburgh, Pittsburgh, Pennsylvania, developed and fabricated the rapid scanning spectrometers and the langmuir microprobe module. Data analyses and manuscript preparation were performed at the Institute for Defense Analyses, Alexandria, Virginia.

References

[1]Erdman, P. W., Zipf, E. C., Espy, P. J., Howlett, C., Levin, D. A., Loda, R., Collins, R. J., and Candler, G. V., "Flight Measurements of Low Velocity Bow Shock Ultraviolet Radiation," *Journal of Thermophysics and Heat Transfer*, Vol. 7, No. 1, 1993, pp. 37–41.

[2]Levin, D. A., Candler, G. V., Collins, R. J., Erdman, P. W., Zipf, E. C., Espy, P. J., and Howlett, C., "Comparison of Theory with Experiment for the Bow Shock Ultraviolet Rocket Flight," *Journal of Thermophysics and Heat Transfer*, Vol. 7, No. 1, 1993, pp. 30–36.

[3]Erdman, P. W., Zipf, E. C., Espy, P. J., Howlett, C., Levin, D. A., Collins, R. J., and Candler, G. V., "In-Situ Measurements of UV and VUV Radiation from a Rocket Plume and Re-Entry Bow Shock," AIAA Paper 92-0124, Jan. 1992.

[4]Candler, G. V., Levin, D. A., Brandenberg, J., Collins, R. J., Erdman, P. W., Zipf, E. C., and Howlett, C., "Comparison of Theory with Plume Radiance Measurements from the Bow Shock Ultraviolet 2 Rocket Flight," AIAA Paper 92-0125, Jan. 1992.

[5]Levin, D. A., Candler, G. V., Collins, R. J., Erdman, P. W., Zipf, E. C., and Howlett, C., "Examination of Ultraviolet Radiation Theory for Bow Shock Rocket Experiments—I," *Journal of Thermophysics and Heat Transfer*, Vol. 8, No. 3, 1994, pp. 447–452.

[6]Levin, D., Braunstein, M., Candler, G., Collins, R., and Smith, G., "Examination of Theory for Bow Shock Ultraviolet Rocket Experiments—II," *Journal of Thermophysics and Heat Transfer*, Vol. 8, No. 3, 1994, pp. 453–459.

[7]Levin, D., Candler, G., Collins, R., Howlett, C., Espy, P., Whiting, E., and Park, C., "Comparison of Theory with Atomic Oxygen 1304Å Radiation Data from the Bow Shock Ultraviolet 2 Rocket Flight," AIAA Paper 93-2811, July 1993.

[8]Rollstin, L., private communication, Sandia National Lab., Albuquerque, NM, March 1992.